Energetic Particle Transport and Loss Induced by Helically-trapped Energetic-ion-driven Resistive Interchange Modes in the Large Helical Device

K. Ogawa[1,2], M. Isobe[1,2], S. Sugiyama[3], H. Matsuura[3], D. A. Spong[4], H. Nuga[1], R. Seki[1,2], S. Kamio[1], Y. Fujiwara[1], H. Yamaguchi[1], M. Osakabe[1,2], and LHD Experiment Group[1]

[1]National Institute for Fusion Science, National Institutes of Natural Sciences, Toki, 509-5292, Japan.

[2]The Graduate University for Advanced Studies, SOKENDAI, Toki, 509-5292, Japan.

[3]Kyushu University, Fukuoka, 819-0395, Japan.

[4]Oak Ridge National Laboratory, Oak Ridge, Tennessee, 37831, USA.

kogawa@nifs.ac.jp

Abstract

In this work, energetic-ion confinement and loss due to energetic-ion driven magnetohydrodynamic modes are studied using comprehensive neutron diagnostics and orbit-following numerical simulations for the Large Helical Device (LHD). The neutron flux monitor is employed in order to obtain global confinement of energetic ions and two installed vertical neutron cameras (VNCs) viewing different poloidal cross-sections are utilized in order to measure the radial profile of energetic ions. A strong helically-trapped energetic-ion-driven resistive interchange mode (EIC) excited in relatively low-density plasma terminated high-temperature state in LHD. Changes in the

neutron emission profile due to the EIC excitation are clearly visualized by the VNCs. The reduction in the neutron signal for the helical ripple valley increases with EIC amplitude, which reaches approximately 50%. In addition to the EIC experiment, orbit-following simulations using the DELTA5D code with EIC fluctuations were performed to assess the energetic-ion transport and loss. Two-dimensional temporal evolution results show that the neutron emissivity at the helical ripple decreases significantly due to the EIC. The rapid reduction in neutron emissivity shows that the helically-trapped beam ions immediately escape from the plasma. The reduction in the VNC signals for the helical ripple valley and the total neutron emission rate increase with increasing EIC amplitude, as observed in the experiment. Calculated line-integrated neutron emission results show that the profile measured by VNC1 has one peak, whereas the profile measured by VNC2 has two peaks, as observed in the experiment. Although the neutron emission profile for VNC2 has a relatively wide peak compared with the experimental results, the significant decrease in neutron signal corresponding to the helical ripple valley was successfully reproduced.

1. Introduction

A sustained high-temperature and high-density plasma is required to realize a nuclear fusion reactor. The confinement of deuterium(D)–tritium(T) fusion-born alpha particles is a critical issue because the fusion-burning plasma is primarily sustained by self-heating via alpha particles. Alpha particle confinement will be one of the main topics studied in ITER [1]. In current fusion devices, the

confinement of energetic ions, such as beam ions, ion cyclotron-heated tail ions, and fusion-born triton has been studied instead of alpha particle confinement.

Energetic particle confinement has been intensively studied in tokamaks using neutral beam injection and ion cyclotron heating [2]. In particular, energetic-ion transport/loss due to the energetic-ion-driven magnetohydrodynamic (MHD) mode has been studied to prevent significant energetic-ion loss, which may cause a localized heat load to damage the plasma-facing components, such as first wall. For example, energetic particle modes, such as the fishbone instability found in Princeton Beta Experiment [3], are excited by a steep gradient of trapped energetic particles caused by high-power neutral beam injection. In studies on the effect of the energetic particle mode on energetic-ion confinement, neutron diagnostics play an important role because neutrons from neutral beam-heated plasmas primarily arise from beam–thermal reactions [4]. In intermediate-sized tokamaks, a large, sudden reduction in the neutron emission rate due to the fishbone instability has been measured by plastic scintillation detectors at the DIII-D [5] and ASDEX Upgrade [6], which showed degradation in the global beam ion confinement. For large tokamaks, the redistribution of energetic ions due to energetic particle modes has been observed using a neutron camera at JT-60U [7]. At the TFTR, it has been reported that the peak of the DT neutron emission profile is altered by fishbone instability in the DT discharge [8].

Research in stellarators and helical devices, which have the advantage of steady-state plasma operation, is also advancing toward the realization of fusion reactors [9-12]. One issue in this

field is energetic particle confinement in stellarators and helical devices. However, a recent energetic-ion confinement study based on NBs and ICRFs in stellarators and helical devices demonstrated potential for alpha particle confinement [13-16]. MHD mode-induced transport and loss of energetic ions have been studied with intense NB injections at the Large Helical Device (LHD) [17, 18]. Relevant hydrogen experiments are primarily performed by charge-exchanged neutral diagnostics using E||B, compact, Si, and natural diamond neutral particle analyzers [19] as well as escaping beam ion diagnostics using a fast-ion-loss detector [20, 21]. In addition to energetic-particle-driven MHD mode-induced beam ion transport/loss, bulk-plasma-pressure-driven MHD modes and resonant magnetic perturbations have been reported to induce beam ion transport/loss [22-28]. Numerical simulations based on the MEGA code have qualitatively reproduced experimental observations [29, 30]. Although our understanding of energetic particle confinement has been broadened by these studies, local measurements of charge-exchanged fast-neutral and escaping energetic ions are limited.

Our understanding of energetic particle confinement has been greatly enhanced by the deuterium operation at the LHD, which began in March 2017 [31]. Neutron diagnostics, such as a neutron flux monitor (NFM) [32], neutron activation system [33], vertical neutron camera (VNC) [34], neutron fluctuation detector [35], and scintillating-fiber detector [36] have been installed for the deuterium operation at the LHD, as powerful tools for elucidating the behavior of confined energetic ions because neutrons created in the neutral beam-heated deuterium plasma at the LHD primarily

arise from the so-called beam–thermal reaction [37]. In the first campaign of the LHD deuterium experiment, initial neutron diagnostics were performed [38-40]. A short pulse beam injection experiment demonstrated that the confinement of beam ions in an MHD quiescent plasma can be described using neoclassical models. In addition, a DD fusion-born 1 MeV triton burnup experiment showed that the burnup ratio of 1 MeV triton is comparable to that obtained at the ASDEX Upgrade [41] and KSTAR [42], whose minor radii are comparable to that of the LHD. A similar triton burnup experiment is being planned for a future deuterium experiment at Wendelstein 7-X [43].

The helically-trapped energetic-ion-driven resistive interchange mode (EIC) [44, 45] is often excited in high-temperature discharges in relatively low-density plasma experiments by intense perpendicular neutral beam injections. The maintenance of this high-ion-temperature state is limited by the EIC [46]. The EIC is destabilized by the resonant interaction of helically-trapped beam ions located at the plasma edge with a poloidal and toroidal mode number of 1. Thus, the EIC characteristics have been studied [47], and EIC control based on an electron cyclotron heating/current drive are currently being tested [48]. In the first deuterium campaign at the LHD, neutron emission profile changes due to the EIC were observed by VNC1 [49, 50]. Although the change in the line-integrated neutron emission profile caused by the EIC was successfully measured, the neutron count was not sufficient because VNC1 is designed to measure the neutron emission profile with a total neutron emission rate of 10^{16} n/s, which is the expected maximum total neutron emission rate for the LHD [37]. In this paper, we present experimental measurements of the neutron

emission profile change caused by the energetic-particle-driven MHD mode and orbit-following simulation results of energetic-ion transport due to the energetic-particle-driven MHD mode at the LHD.

2. Experimental setup

Energetic-ion transport due to the EIC was studied at the LHD. The LHD is one of the largest helical devices in the world, with a major radius of 3.9 m and an average minor radius of 0.6 m [31]. Figure 1 (a) shows a bird's eye view of the LHD. Three negative-source-based NBs (NNB) and two positive-source-based NBs (PNB) have been installed at the LHD [51], with typical acceleration voltages of 180 keV and 60–80 keV, respectively. Note that both PNBs primarily produce helically-trapped beam ions in one of two helical ripple valleys, as shown in Fig. 1 (a). A high-pressure gradient of helically-trapped beam ions to excite the EIC can be easily created with the PNB geometry. Figure 1 (b) shows the comprehensive neutron diagnostic tools installed at the LHD.

In this experiment, we primarily used the NFM and VNCs. An absolutely calibrated NFM which consists of three fission chambers, one ^{10}B detector, and two ^{3}He detectors were installed on the top and the equatorial plane of the LHD, as shown in Fig. 1 (a). The fission chamber installed on the top acts as a primary detector to measure the total neutron emission rate and yield for both research purposes and radiation management at the LHD. The time response and time resolution of the fission chamber are 2 ms and 0.5 ms, respectively, due to the cutting-edge digital

signal-processing units based on a field-programmable gate array (FPGA) developed by the National Institute for Fusion Science and Toshiba Energy Systems & Solutions Corporation [52]. Two neighboring VNCs (VNC1 [53] and VNC2) were installed on the lower diagnostics ports at the basement level of the LHD torus hall. Figures 2 (a) and (b) show poloidal cross-sections of VNC1 and VNC2, respectively. The multichannel collimators of both VNCs are composed of hematite-doped heavy concrete with a weight density of approximately 3.5 g/cc to provide superior gamma-ray shielding performance, as proven by MCNP6 calculations and 800 MBq ^{252}Cf experiments [54, 55]. The number of hole and inner diameter are 11 and 30 mm for VNC1 and 9 and 50 mm for VNC2, respectively. A larger inner diameter is employed for VNC2 to obtain relatively high statistics in measuring the neutron emission profile at relatively low neutron rate discharges, such as those encountered in EIC discharges. Eight of the eleven detectors for VNC1 are located at an R of 3.63 m, 3.72 m, 3.82 m, 3.91 m, 3.99 m, 4.08 m, 4.17 m, and 4.26 m, and the nine detectors for VNC2 are located at an R of 3.34 m, 3.42 m, 3.50 m, 3.64 m, 3.73 m, 3.82 m, 3.95 m, 4.02 m, and 4.09 m. In addition, a chemical vapor-deposited artificial diamond-based neutral particle analyzer was tandemly installed with VNC2 [56]. A stilbene scintillator with a diameter of 20 mm and a thickness of 10 mm coupled with a high-gain stability photomultiplier tube (H13698-01, i.e., a modified version of H11934-100-10, Hamamatsu Photonics K.K [57]) was utilized as the fast neutron detector for VNC1. The anode signal of the stilbene detector is directly fed into a data acquisition system equipped with a 14 bit/1 GHz analog-to-digital converter with an FPGA and 1 GB

of dynamic random access memory (APV8102-14MWPSAGb, Techno AP [58]). For VNC2, an EJ-410 [59] fast neutron detector with a diameter of 2 inches and a thickness of 0.625 inches is coupled with a 2-inch photomultiplier tube (H7195, Hamamatsu Photonics K.K [60]). Notably, EJ-410, which has a higher sensitivity to fast neutrons and a lower sensitivity to gamma rays as an improved version of NE451, was used at the TFTR [61]. The anode signal of EJ-410 is fed into a current amplifier (C7319, Hamamatsu Photonics K.K [62]), with a cutoff frequency and gain of 20 kHz and 10^5, respectively. The output signal of C7319 is acquired by a 12 bits/1 MHz analog-to-digital converter (PXI6133, National Instruments [63]). The relative gain of VNC2 is adjusted using a ^{137}Cs gamma-ray source. We adjusted the high voltage of the photomultiplier tube of each EJ-410 detector to match the number of gamma-ray counts for the ^{137}Cs gamma-ray source located in front of each detector at the same distance. One of the major differences between the two VNCs is their toroidal location. VNC1 is placed at a vertically elongated poloidal cross-section, whereas VNC2 is placed at a diagonal poloidal cross-section. Figures 2 (c) and (d) illustrate why a diagonal cross-section was chosen for VNC2. These figures show the line of sight for VNC1 and VNC2 and the typical beam ion density in the PNB-heated plasma, calculated using the MORH code, which is based on a five-dimensional drift kinetic model with linear Coulomb collisions [64]. The PNB primarily produces helically-trapped beam ions, which move along the valley of the helical ripple formed by two twisted coils of the LHD. Therefore, the density profile of the helically-trapped beam ions has a poloidal structure. VNC2 was designed to complement VNC1 in obtaining the

poloidal structure of the PNB ions. Note that existence of super-banana particles, which is a kind of helically-trapped ion, confined between the inner sides of two helical coils is predicted in particular magnetic configuration by numerical simulation [65]. The orbit of super-banana particle is unstable because the particle stays quite local region.

3. Experimental results

For high-ion-temperature discharge, the EIC was excited at a B_t of 2.85 T and an R_{ax} of 3.60 m (Fig. 3), where toroidal magnetic field is in counter-clockwise direction when viewed from above. In this discharge, three NNBs simultaneously inject hydrogen beams, whereas two PNBs inject deuterium beams. Therefore, neutrons are primarily created by reactions between helically-trapped ions injected by the PNB and bulk deuteron. The temporal evolution of the central electron temperature (T_{e0}) was measured by Thomson scattering [66], with a T_{e0} of approximately 3 keV throughout the discharge. The maximum central ion temperature (T_{i0}) was measured by charge-exchange recombination spectroscopy (CXRS) [67] at approximately 9 keV. The line-averaged density (n_{e_avg}) measured by interferometer [68] rapidly increased at t = 4.63 s due to the carbon pellet injection [69]. The plasma-stored energy (W_p) was measured by a diamagnetic coil [70], with a W_p of approximately 800 kJ during the PNB injection. The temporal evolution of the magnetic fluctuation amplitude, as measured by a Mirnov coil placed on a vacuum vessel [70], shows that EIC bursts occurred at t = 4.74 s and 4.86 s. A sudden reduction in the total neutron

emission rate (S_n), as measured by the NFM, and reductions in the line-averaged density and W_p were observed in association with the EIC, as reported in Ref. 50. Here, the decrease in T_{i0} at t = 4.75 s may be due to the transport/loss of helically-trapped beam ions, induced by the EIC. Figure 4 (a) shows the temporal evolution of the EIC fluctuation amplitude measured by the Mirnov coil, the neutron counts averaged over 10 ms measured by VNC1, and the neutron signal measured by VNC2. Here, we applied a digital low-pass filter with a cutoff frequency of 50 kHz to the Mirnov coil signal in order to more clearly display the EIC burst. The horizontal and vertical error bars for the VNC1 data indicate the statistical error and time bin size, respectively. For the VNC2 data, 2000 point data smoothing was applied. A significant reduction in the neutron signal can be observed for S_n, the central channels (R = 3.72 m and 3.81 m) of VNC1, and the outer channels (R = 3.80 m and 3.95 m) of VNC2. The change in signals of S_n, one of the central channels of VNC1 (R=3.72 m), and one of the outer channels of VNC2 (R of 3.95 m) as a function of the EIC fluctuation amplitude is shown in Fig. 4 (b), where the signal reduction is defined as the signal decrease during the EIC burst divided by the signal before the EIC burst. The reduction for the S_n, VNC1 counts, and VNC2 signal due to the EIC increased with increasing peak EIC amplitude, as measured by the Mirnov coil, reaching 50%.

Line-integrated neutron emission profiles before and after the EIC discharge were obtained by VNC1 and VNC2 (Fig. 5). Here, we integrated the VNC1 neutron counts over 20 ms and averaged the VNC2 neutron signal over 20 ms. The vertical error bar for VNC1 is based on the count statistics,

whereas the vertical error bar for VNC2 is based on the signal fluctuations. The line-integrated neutron emission profile for VNC1 has a relatively broad peak at an R of approximately 3.75 m, corresponding to the helical ripple valley. Prior to the EIC burst, the neutron count at the peak position was approximately 170. However, the count increased to approximately 100 after the EIC burst. Due to the EIC, the neutron count in the central channel was reduced by almost one half. However, the neutron counts for the edge channel remained nearly constant for VNC1. The line-integrated neutron emission profile exhibits two narrow peaks at R values of approximately 3.4 m and 4.0 m. These peak positions correspond to helical ripple valleys located on the inboard and outboard sides of the LHD. Prior to the EIC burst, the neutron signal at the peak position was approximately 0.15 V. However, the counts reached approximately 0.1 V after the EIC burst. The neutron signals at the two peaks decreased to almost 2/3, whereas the neutron signal in the central channels only had a slight decrease. These experimental results clearly confirm that the neutron emission profiles were strongly influenced by the EIC.

4. Setup for orbit-following calculations with EIC fluctuations

To investigate the effect of the EIC on helically-trapped beam ion confinement and loss, orbit-following simulations with EIC fluctuations were performed. Figure 6 shows a flowchart for the orbit-following simulation. In the simulation, we used the electron temperature profile, electron density profile, and ion temperature profile measured in the experiment. The deuteron profile was

evaluated from the carbon density measured by CXRS and the deuteron dilution measured by visible spectroscopy [71]. In this discharge, the carbon density in the plasma core region was approximately 4×10^{17} m^{-3}, and the D/(H+D) and (H+D)/He ratios were ~0.6 and more than 0.9, respectively. A three-dimensional plasma equilibrium was reconstructed by VMEC2000 in the fixed-boundary mode [72]. The birth positions of the PNB ions were calculated by the HFREYA code, which is part of the FIT3D-DD code [73, 74]. Based on the equilibrium and birth positions, we followed the PNB ions in Boozer coordinates using the DELTA5D code with EIC fluctuations [75]. It is worth noting that DELTA5D code has been applied at the LHD to reproduce toroidal Alfvén eigenmode-induced energetic-ion loss [25]. We judge that the PNB ion is lost when the ion reaches the last closed flux surface. The energy and three-dimensional space distribution of energetic ions are output every 0.5 ms. The neutron emission profile at the poloidal cross-section in which the VNCs are located was calculated using the energetic-ion distribution calculated with DELTA5D. The cross-section of the beam–plasma fusion reaction was calculated from the beam–target fusion reactivity [76] and the fusion cross-section described in Ref. 77. Figure 7 shows the radial profiles of T_e, T_i, n_e, and n_i used in this calculation. The density and electron temperature profiles have relatively broad shapes, whereas the ion temperature profile exhibits a narrower peak. We included EIC fluctuation from t of 4.860 s to 4.862 s. The EIC fluctuation was assumed as $\boldsymbol{b} = \nabla(\alpha\times\boldsymbol{B})$ with $\alpha = 1/\omega\times(n\text{-}m\iota)/(g+I\iota)\phi$, where the radial profile of the eigenfunction ϕ is based on the radial profile of the EIC measured by the ECE [45, 78]. The peak and 1/e width of ϕ correspond to r/a values of 0.85 and 0.1, respectively.

The EIC frequency is decreased from 10 kHz to 5 kHz over 2 ms, as observed in the experiment. Moreover, the toroidal and the poloidal mode numbers were set to be 1, as observed in the experiment. In particular, the peak location of the EIC corresponds to the location of the rotational transform of 1. The EIC amplitude at the Mirnov coil position ($b_{\theta\_\mathrm{EIC\_cal}}$) was estimated by assuming a simple cylindrical plasma, as described in Ref. 25.

5. Orbit-following simulation results

Figures 8 (a) and (b) show the neutron emissivity for the poloidal cross-sections at which VNC1 and VNC2 are located for a $b_{\theta\_\mathrm{EIC\_cal}}$ of approximately 10^{-3} T. In this figure, the gray lines show the line of sight for the VNCs, and the line width corresponds to the inner diameter of the multichannel collimator. The red region corresponds to a neutron emissivity of 1×10^{13} $\mathrm{m^{-3}s^{-1}}$, whereas the dark blue region corresponds to a neutron emissivity of 5×10^{11} $\mathrm{m^{-3}s^{-1}}$. Figures 8 (c) and (d) show the temporal evolution of the relative counts for VNC1 and the relative neutron signal for VNC2 obtained from the numerical simulation. In this calculation, one PNB (NB5) injects a deuterium beam with an acceleration voltage of 68 keV at t = 4.70 s, whereas another PNB (NB4) injects a deuterium beam with an acceleration voltage of 59 keV for t = 4.80–4.88 s. An EIC burst was implemented at t = 4.86–4.862 s. As shown by the two-dimensional neutron emissivity profile, the neutron emissivity at the helical ripple valley increases with time and then rapidly decreases due to the EIC fluctuation. The neutron emissivities at the lower helical ripple shown in Fig. 8 (a) and the

upper right helical ripple shown in Fig 8(b) are higher than those of the other helical ripple because the two PNBs injected ions into the same helical ripple valley. The neutron signals shown in Fig. 8 (c) and (d) gradually increase with the injection of NB4. In Fig. 8 (c), the neutron signals at R = 3.72 m and 3.82 m show relatively high counts compared with the other channels, followed by a sudden decrease due to the EIC. The signals from the central channel region, for example, at R = 3.72 m and 3.82 m, are decreased by almost one half. In contrast, the signal of the edge channel region, for example, at R = 3.99 m, shows little change. In Fig. 8 (d), the neutron signals at R = 3.95, 4.02, 3.50, and 3.42 m are relatively large compared with the other channel signals. The calculation results for t = 4.800–4.864 s show that the helically-trapped beam ions are instantly lost due to the EIC, and this loss stops immediately after the EIC burst. As shown in Fig. 7 (b), the EIC is located at the edge of the plasma, and the eigenfunction expands toward the last closed flux surface. Due to this EIC structure, the helically-trapped beam ions can be easily transported to the last closed flux surface, instead of remaining in the plasma-confined region. The temporal evolution of S_n, the VNC1 signal at R = 3.72 m, and the VNC2 signal at R = 3.95 m are shown in Fig. 9 (a). In this calculation, EIC amplitudes of 0, 2×10^{-4}, 4×10^{-4}, and 1×10^{-3} T were applied. The reductions in the S_{n_cal} and VNC signals increase with increasing EIC amplitude. The decay time of S_{n_cal} is nearly equivalent to the decay times for VNC1 and VNC2. The signal immediately decreases when the EIC is applied and then stops when it is halted. We have four time bins during EIC fluctuation. The reduction ration in S_n in each time bin is 11%, 17%, 9%, and 5%. We observed relatively large reduction rate in second

time bin whereas only 5% reduction was observed in forth time bin. The difference of reduction in each time bin thought to be due to EIC frequency. It is worth noting that the reduction ratio becomes small when EIC frequency is fixed. The signal reduction is plotted as a function of EIC amplitude in Fig. 9 (b), showing that the signal decreases almost linearly as the EIC amplitude increases. Here, the signal reduction rate obtained in DELTA5D simulation is comparable with the reduction rate in experiment as shown in Fig. 9 (c). This linear dependence indicates that the dominant loss process is convective [79, 26]. The helically-trapped beam ions existing near the loss boundary are immediately lost due to the EIC fluctuation. A convective-type process is consistent with instant loss of helically-trapped beam ions due to EIC indicated by two-dimensional image of neutron emissivity.

Figure 10 (a) and (b) shows the line-integrated neutron profile obtained from the numerical simulation. As observed in the experiment, the neutron emission profile for VNC1 exhibits a peak. This peak occurs at R = 3.7–3.8 m, which is nearly equivalent to the experimental result. After the EIC burst, the neutron counts at the central channel (R = 3.6–3.9 m) decreased by almost 50%, as observed in the experiment. Although the neutron profile for VNC2 has a relatively wide peak, the calculated line-integrated neutron emission exhibits two peaks, with a decrease after the EIC burst as shown in Fig. 10 (c) and (d). A significant decrease in the neutron signal due to the EIC burst at the outboard peak (R = 3.95 and 4.02 m) is observed, whereas the decrease in the neutron signal due to the EIC burst at the inboard peak (R = 3.42 and 3.50 m) is relatively small. This relatively small decrease for the inboard peak may be due to super-banana particles [65] confined in a relatively

small r/a region compared with the helically-trapped beam ions. The third largest region for the two-dimensional neutron emissivity is observed at Z = -0.20 and R = ~ 3.5 m, as shown in Fig. 8 (b). This region corresponds to super-banana particles confined between the inner sides of two helical coils. The EIC has little effect on such super-banana particles because these particles exist in a relatively small r/a region compared with the EIC. These super-banana particles can arise in numerical simulations. However, the confinement of super-banana particles is thought to be undesirable in experiments because their trajectories deviate substantially from the flux surface [65]. The reduction in the inboard peak becomes larger when super-banana particles are not considered. Comparison between experimental results with numerical simulation based on real coordinate including open field region and including wave-particle interaction remains as future work.

6. Summary

The effect of the EIC on helically-trapped energetic-ion confinement was studied via experiments and orbit-following simulations. A significant reduction in the neutron signal of the NFM and two VNCs was observed due to the EIC. The reduction in the NFM and VNC signals increased with increasing EIC amplitude measured by a Mirnov coil, reaching 50%. Line-integrated neutron profiles obtained before and after the EIC burst showed that the neutron signal corresponding to the helical ripple valley decreased significantly. Orbit-following simulations using the DELTA5D code with EIC fluctuation were performed to evaluate the transport/loss of helically-trapped beam ions due to

EIC. The temporal evolution of the two-dimensional neutron emissivity showed that the neutron emission in the helical ripple valley suddenly vanished due to the EIC, indicating that the helically-trapped beam ions are immediately lost. Calculated line-integrated neutron emission profiles qualitatively agree with the experimentally obtained neutron emission profiles.

Acknowledgements

This research was partly supported by NIFS Collaboration Research programs (KOAH037), and by the LHD project budget (ULHH003, ULHH034, and ULGG801). This work was also partly supported by JSPS KAKENHI Grant Number C19K03798.

[1] Fasoli A. et al 2007 Nuclear Fusion **47** S264.

[2] Heidbrink W. W. and Sadler G. J. 1994 Nucl. Fusion **34** 535.

[3] Heidbrink W. W. et al 1986 Phys. Rev. Lett. **57** 835.

[4] Wolle B. 1999 Phys. Rep. **312** 1-86.

[5] Heidbrink W. W. and Sager G. 1990 Nucl. Fusion **30** 1015.

[6] Kass T. et al 1998 Nucl. Fusion **38** 807.

[7] Ishikawa M et al 2005 Nucl. Fusion **45** 1474.

[8] Goeler S. von et al 1996 Rev. Sci. Instrum. **67** 473.

[9] Takeiri Y. 2018 IEEE Trans. Plasma Sci. **46** 2348.

[10] Osakabe M. et al 2018 IEEE Trans. Plasma Sci. **46** 2324.

[11] Dinklage A. et al 2018 Nat. Phys. **14** 855.

[12] Wolf R. et al 2019 Phys. Plasmas **26** 082504.

[13] Murakami S. et al 2004 Fus. Sci. Technol. **46** 2 241.

[14] Osakabe M. et al 2004 Fus. Sci. Technol. **46** 131.

[15] Akaslompolo S. et al 2019 JINST **14** C10012.

[16] S. A. Lazerson 2019 "*First neutral beam experiments on Wendelstein 7-X*", 28th International Toki Conference and to be submitted to Plasma and Fusion Research.

[17] Toi K. et al 2010 Fus. Sci. Technol. **58** 186.

[18] Toi K. et al 2011 Plasma Phys. Control. Fusion **53** 024008.

[19] Isobe M. et al 2010 Fus. Sci. Technol. **58** 426.

[20] Ogawa K. et al 2008 Plasma Fusion Res. **3** S1082.

[21] Ogawa K. et al 2009 J. Plasma Fusion Res. SERIES **8** 655.

[22] Osakabe M. et al 2006 Nucl. Fusion **46** S911.

[23] Ogawa K. et al 2010 Nucl. Fusion **50** 084005.

[24] Isobe M. et al 2010 Contrib. Plasma Phys. **50** 540.

[25] Ogawa K. et al 2012 Nucl. Fusion **52** 094013.

[26] Ogawa K. et al 2013 Nucl. Fusion **53** 053012.

[27] Ogawa K et al 2014 Plasma Fusion Res. **9** 3402097.

[28] Ogawa K et al 2014 Plasma Phys. Control. Fusion **56** 094005.

[29] Todo Y. and Sato T. 1998 Phys. Plasmas **5** 1321.

[30] Seki R. et al 2019 Nucl. Fusion **59** 096018.

[31] Takeiri Y. et al 2017 Nucl. Fusion **57** 102023.

[32] Isobe M. et al 2014 Rev. Sci. Instrum. **85** 11E114.

[33] Pu N. et al 2017 Rev. Sci. Instrum. **88** 113302.

[34] Ogawa K. et al 2018 Rev. Sci. Instrum. **89** 095010.

[35] Ogawa K. et al 2018 Plasma and Fusion Research **13** 3402068.

[36] Ogawa K. et al 2018 Nucl. Fusion **58** 034002.

[37] Osakabe M et al 2017 Fusion Sci. Technol. **72** 199.

[38] Isobe M. et al 2018 IEEE Trans. Plasma Sci. **46** 2050.

[39] Isobe M. et al 2018 Nucl. Fusion **58** 082004.

[40] Ogawa K. et al 2019 Nucl. Fusion **59** 076017.

[41] Hoek M., Bosch H. S. and Ullrich W. 1999 "Triton burnup measurement at ASDEX Upgrade by neutron foil activation", IPP-Report IPP-1/320.

[42] Jo J. et al 2016 Review of Scientific Instruments **87** 11D828.

[43] Koschinsky J. P. et al to be submitted to Contributions to Plasma Physics.

[44] Du X. D. et al 2015 Phys. Rev. Lett. **114** 155003.

[45] Du X. D. et al 2015 Nucl. Fusion **56** 016002.

[46] Takahashi H. et al 2018 Nucl. Fusion **58** 106028.

[47] Bando T. et al 2018 Nucl. Fusion **58** 082025.

[48] Du X. D. et al 2017 Phys. Rev. Lett. **118** 125001.

[49] Ogawa K. et al 2018 Nucl. Fusion **58** 044001.

[50] Ogawa K. et al 2018 Plasma Phys. Control. Fusion **60** 044005.

[51] Takeiri Y. et al 2010 Fusion Sci. Technol. **58** 482.

[52] Isobe M. et al 2014 Rev. Sci. Instrum. **85** 11E114.

[53] Ogawa K. et al 2018 Rev. Sci. Instrum. **89** 113509.

[54] Ogawa K. et al 2014 Rev. Sci. Instrum. **85** 11E110.

[55] Kawase H. et al 2019 IEEE Trans. Plasma Sci. **47** 462.

[56] Kamio S. et al 2019 JINST **14** C08002.

[57] https://www.hamamatsu.com/resources/pdf/etd/R11265U_H11934_TPMH1336E.pdf

[58] http://www.techno-ap.com/img/APV8102_14MWPSAGb.pdf

[59] https://eljentechnology.com/products/neutron-detectors/ej-410

[60] https://www.hamamatsu.com/jp/en/product/type/H7195/index.html

[61] Roquemore A. L. et al 1997 Rev. Sci. Instrum. **68** 544.

[62] https://www.hamamatsu.com/resources/pdf/etd/C7319_TACC1014E.pdf

[63] http://www.ni.com/pdf/manuals/371231d.pdf

[64] Seki R. et al 2015 Plasma Fusion Res. **10** 1402077.

[65] Miyamoto K. "Plasma Physics for Controlled Fusion" Springer Series on Atomic, Optical, and Plasma Physics DOI 10.1007/978-3-662-49781-4. Page 410.

[66] Yamada I. et al 2010 Fusion Sci. Technol. **58** 345.

[67] Yoshinuma M. et al 2010 Fusion Sci. Technol. **58** 375.

[68] Akiyama T. et al 2010 Fusion Sci. Technol. **58** 352.

[69] Morita S. et al 2010 Fusion Sci. Technol. **58** 91.

[70] Sakakibara S. et al 2010 Fusion Sci. Technol. **58** 471.

[71] Goto M. et al 2010 Fusion Sci. Technol. **58** 394.

[72] Hirshman S.P. and O. Betancourt 1991 J. Comput. Phys.**96** 99.

[73] Murakami S. et al 1995 Trans. Fusion Technol. **27** 256.

[74] Vincenzi P. et al 2016 Plasma Phys. Control. Fusion **58** 125008.

[75] Spong D.A. et al 2011 Phys. Plasmas **18** 056109.

[76] Mikkelsen D. 1989 Nucl. Fusion **29** 1113.

[77] Bosch S. and Hale G. 1992 Nucl. Fusion **32** 611.

[78] Tokuzawa T. et al 2010 Fusion Sci. Technol. **58** 364.

[79] Sigmar D. J. et al., 1992 Phys. Fluids B **4** 6.

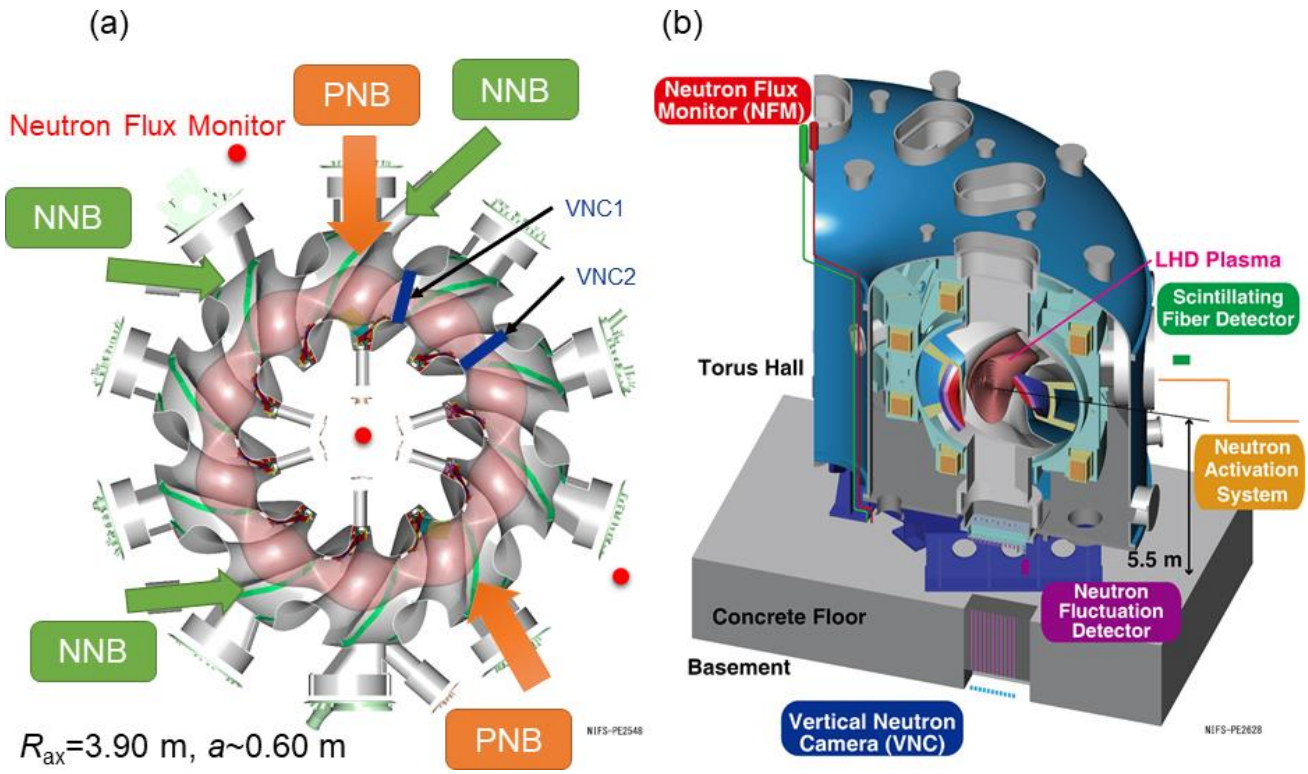

Figure 1 (a). Bird's eye view of the LHD and NBs and the locations of the NFM and VNCs. (b) Comprehensive neutron diagnostics installed at the LHD.

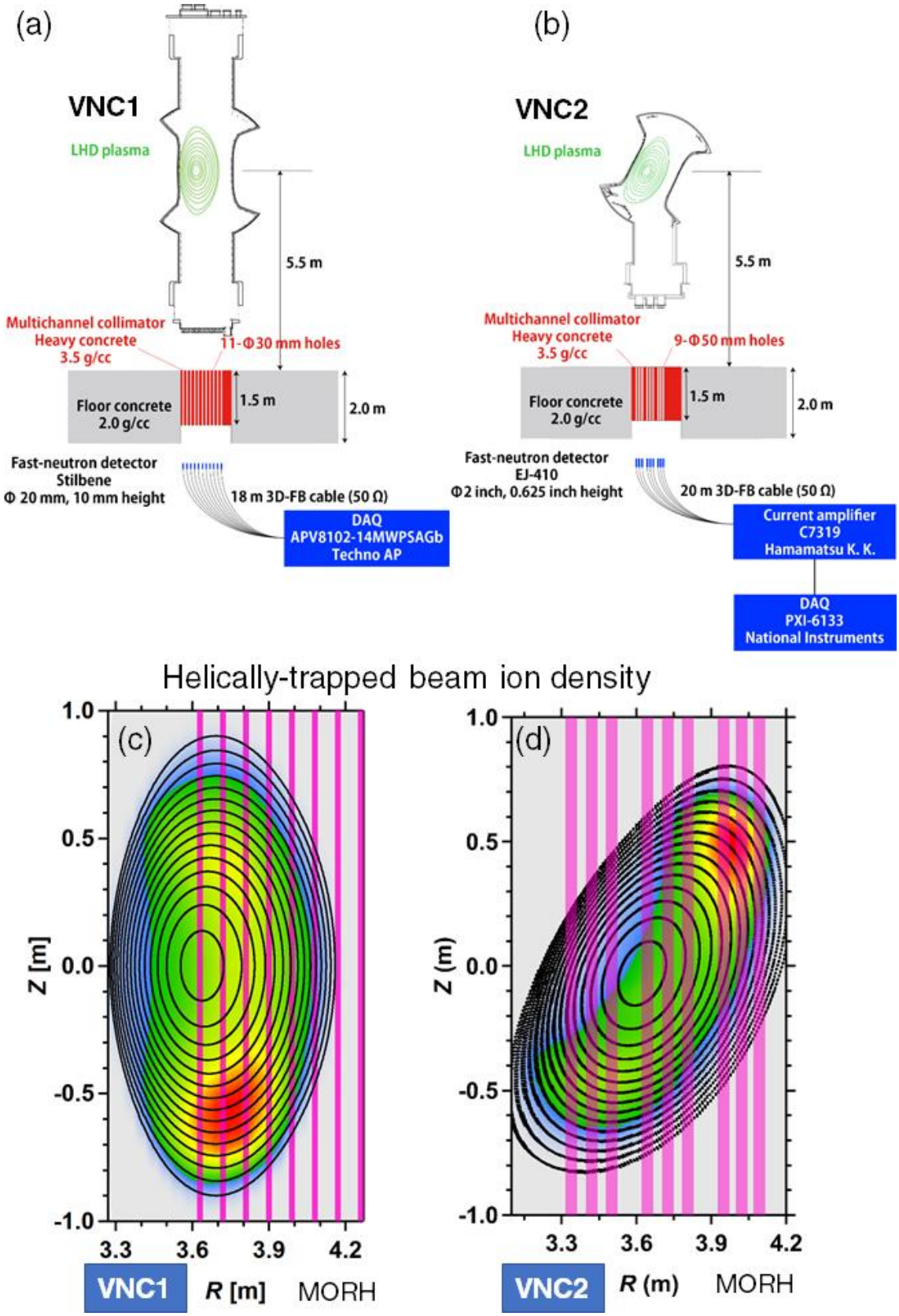

Figure 2. Schematic of (a) VNC1 and (b) VNC2. Line of sight for (c) VNC1 and (d) VNC2 and the typical helically-trapped beam ion density calculated by the MORH code.

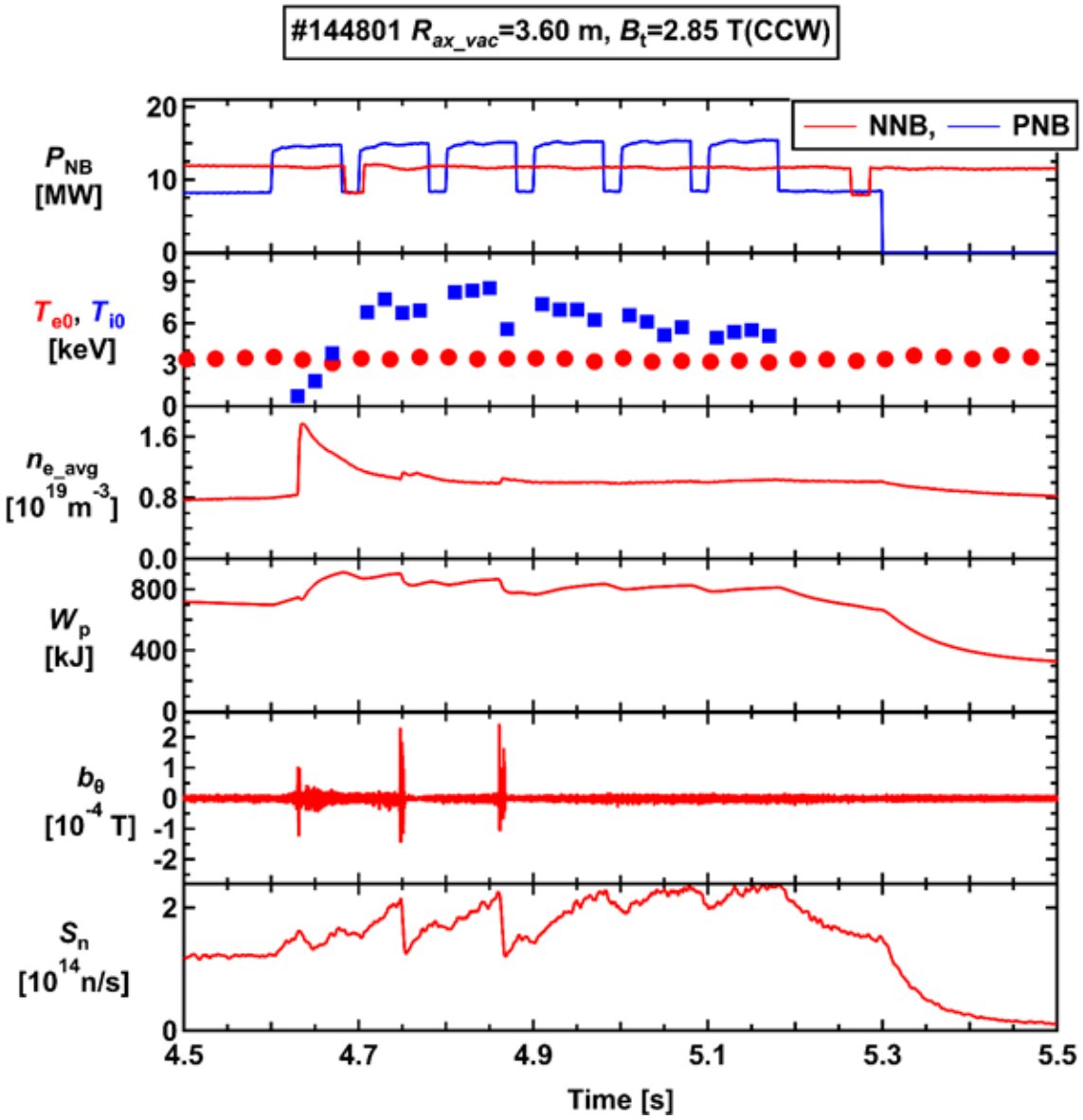

Figure 3. Temporal evolution of high-ion-temperature discharge with the EIC. EIC bursts are clearly seen at t = 4.74 s and 4.86 s.

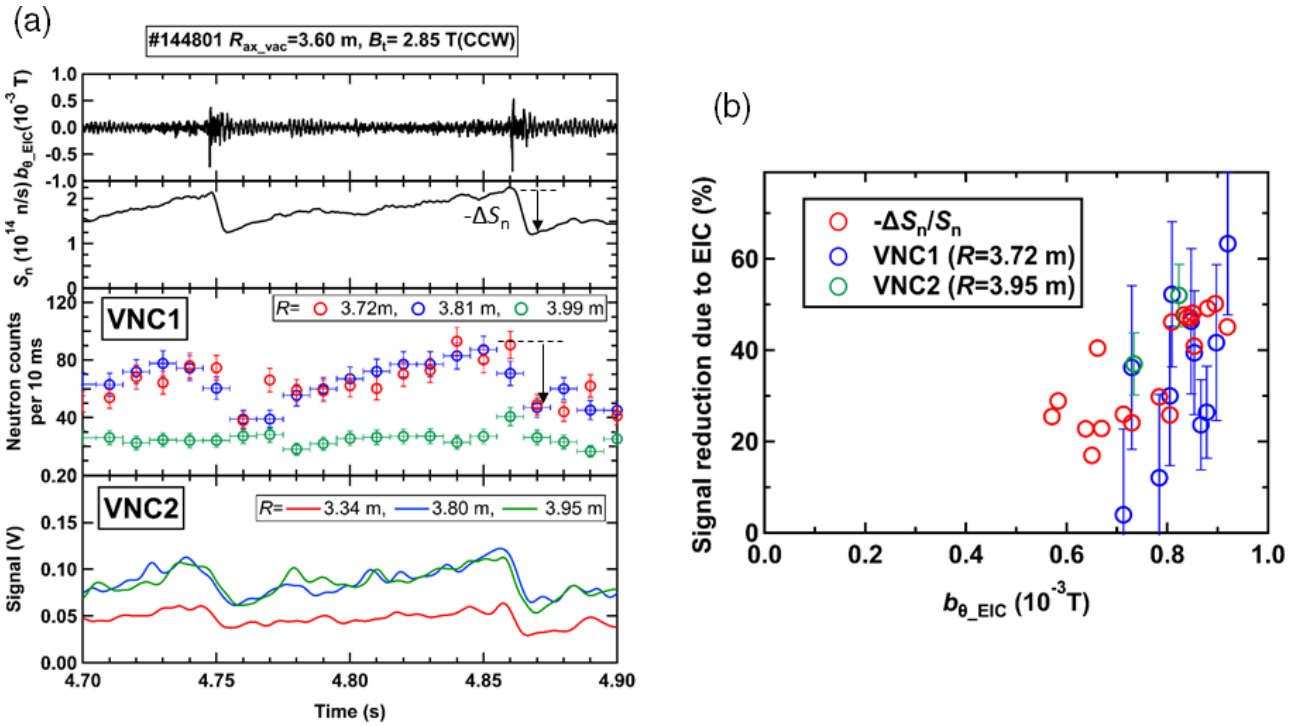

Figure 4 (a). Enlarged temporal evolution of the EIC magnetic fluctuations and neutron signals. (b) Dependence of the reduction in neutron signal due to the EIC burst as a function of the maximum EIC magnetic fluctuation amplitude.

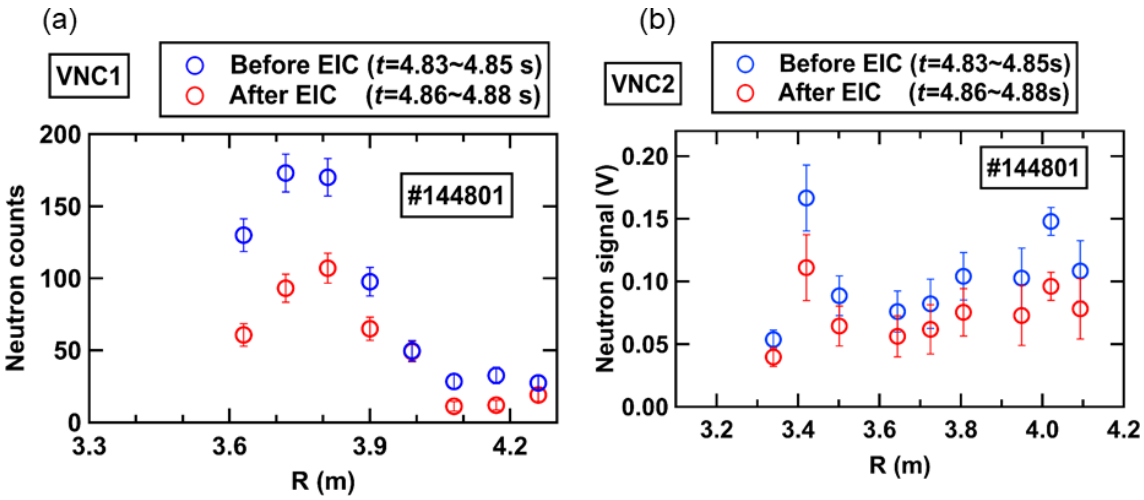

Figure 5. Line-integrated neutron emission profiles before and after the EIC burst for (a) VNC1 and (b) VNC2.

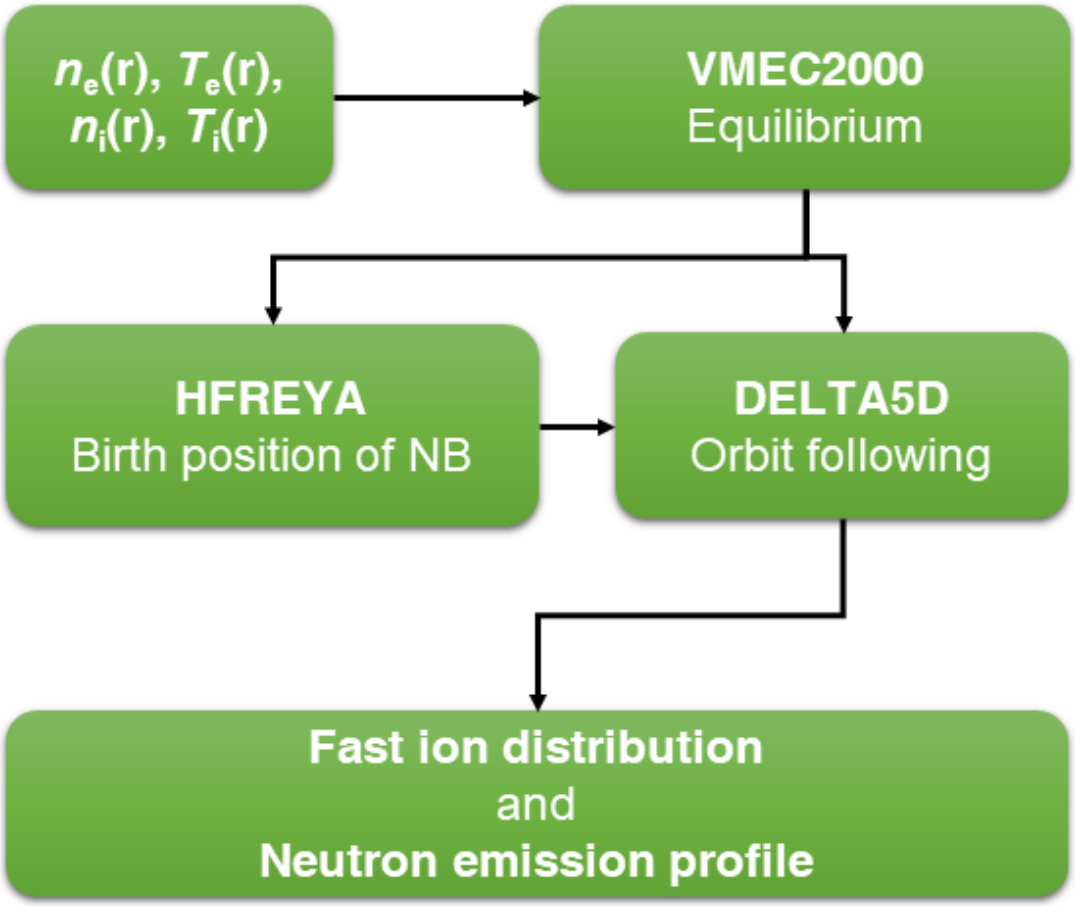

Figure 6. Calculation scheme of the orbit-following simulation with an EIC burst.

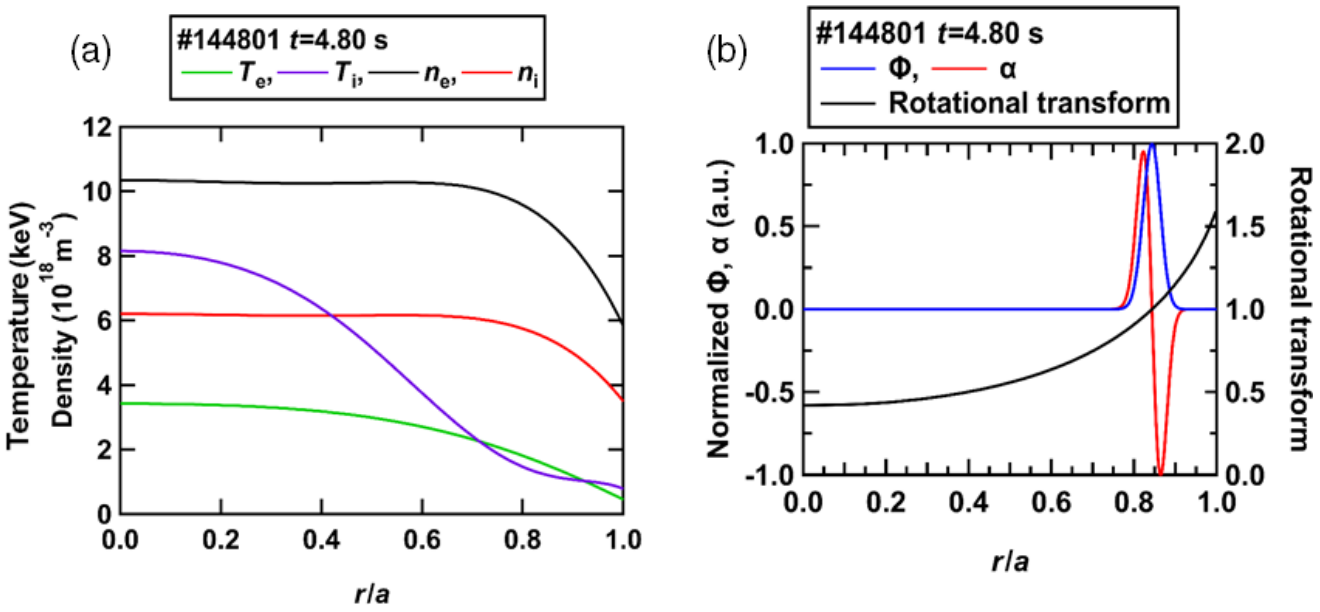

Figure 7. (a) Radial temperature and density profiles used in the simulation. (b) Radial profiles of the eigenfunction, α, and rotational transform.

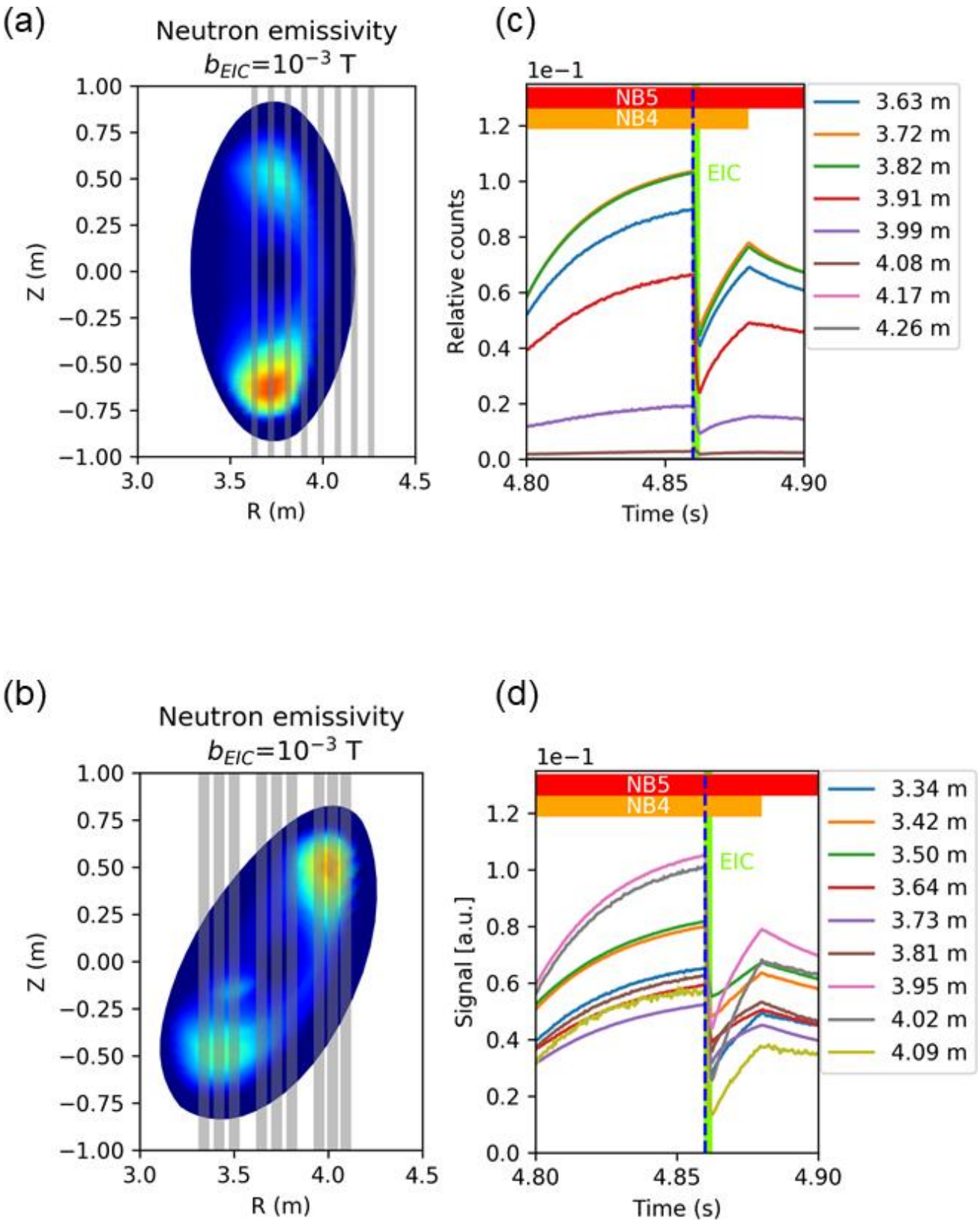

Figure 8. Two-dimensional neutron emissivity in the EIC discharge for (a) VNC1 and (b) VNC2 cross-sections. Time trace of neutron signals for (c) VNC1 and (d) VNC2.

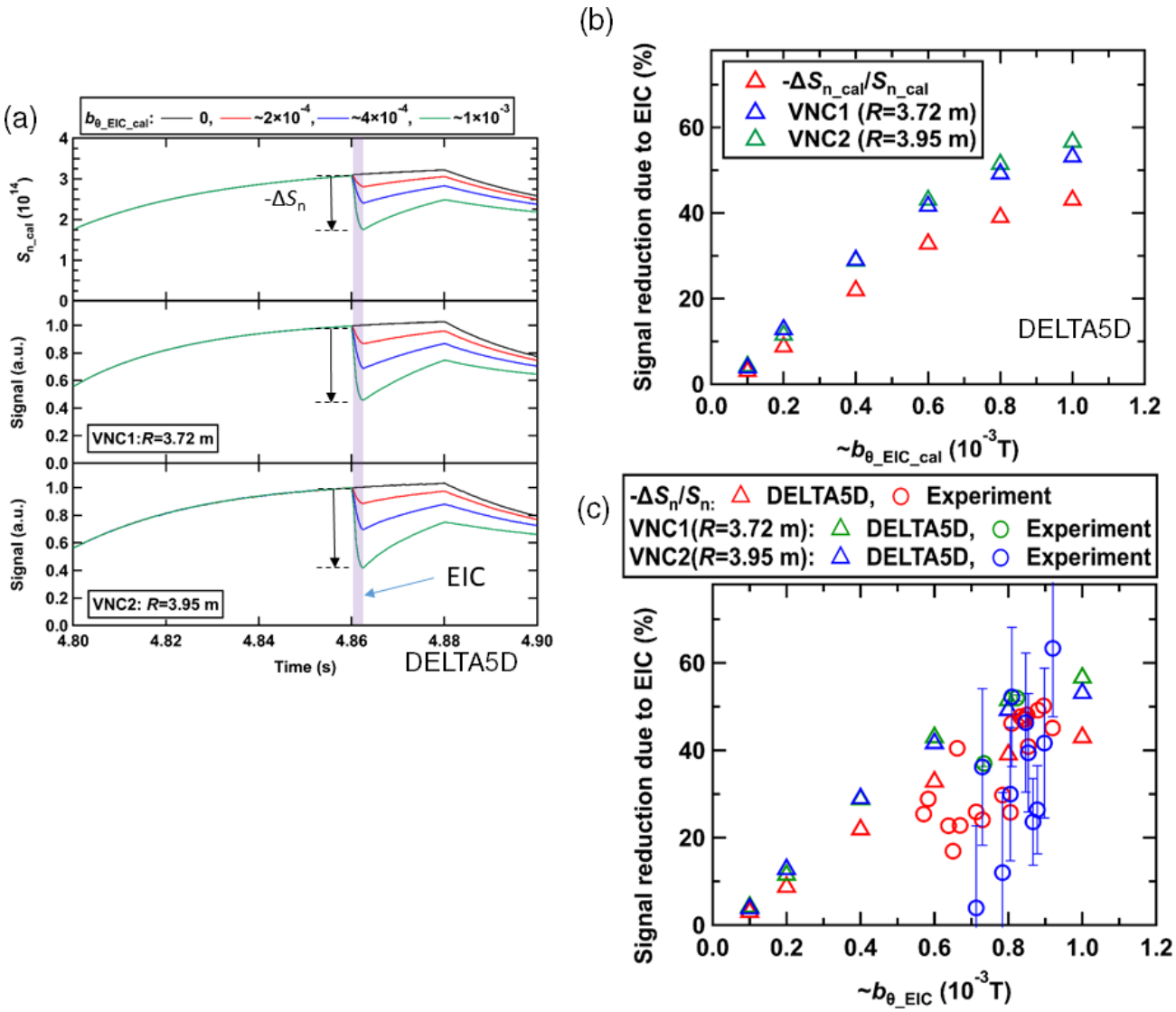

Figure 9. (a) Typical time trace of the total neutron emission rate and VNC signals obtained by numerical simulation. (b) Reduction in S_n and VNC signals as a function of the EIC magnetic amplitude at the Mirnov coil position. (c) Comparison between DELTA5D result with experimental result.

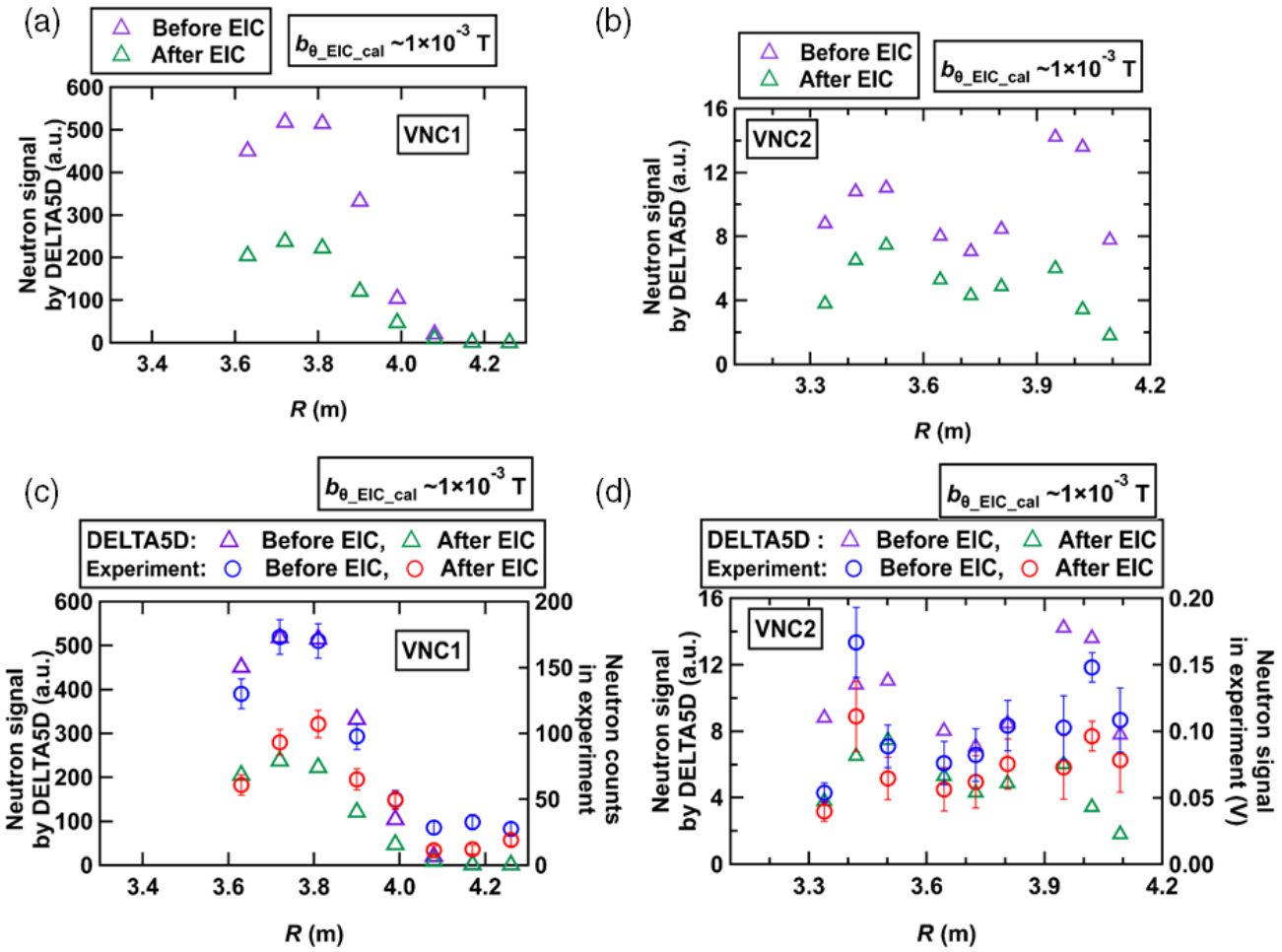

Figure 10. Calculated line-integrated neutron emission profiles before and after the EIC burst obtained for (a) VNC1 and (b) VNC2. Comparison between DELTA5D result with experimental result for (c) VNC1 and (d) VNC2.